Soft Matter

PAPER

View Article Online
View Journal | View Issue

Cite this: *Soft Matter*, 2025, **21**, 6751

Structural complexity driven by liquid–liquid crystal phase separation of smectics

Christopher A. Browne, †[a] Yuma Morimitsu, †[a] Na Kyung Kim,[a] Manesh Gopinadhan,[b] Eric B. Sirota,[b] Ozcan Altintas,[b] Kazem V. Edmond,[b] Paul A. Heiney[c] and Chinedum O. Osuji *[a]

Many phase separated systems—including industrial nanocomposites, biomaterials, and cellular condensates—can form dispersed droplets that exhibit internal liquid crystalline ordering. The elasticity of the internal liquid crystalline mesophase often reshapes the droplet geometry, resulting in structures such as filaments, tactoids, tori, and surface facets. Our recent work demonstrated that by slowly cooling into the binodal from a well-mixed state, the dynamics of this liquid–liquid crystal phase separation (LLCPS) can give rise to striking filamentous networks of smectic condensates. Here, we investigated how choice of mesogen, solvent, and concentration can dramatically alter these networks. Using X-ray scattering, we observed that the solvent swells the smectic layers, seemingly reducing the smectic layer's bend modulus, altering the geometric structure of the network. Consistent with this interpretation, samples with a higher smectic layer swelling exhibited more geometrically-complex structures that require higher smectic layer bending to form. We further demonstrated that the formation of filaments and networks does not occur in all systems exhibiting coexistence of a smectic and isotropic phase. Instead, we only observed filament and network formation when the smectic phase developed directly from the isotropic phase—further highlighting the importance of path-dependence in forming these non-equilibrium structures. These results demonstrate some of the structural diversity of dispersed droplet geometries that can be accessed by LLCPS, and elucidate some of the requisite conditions for them to form networked morphologies.

Received 12th May 2025,
Accepted 30th July 2025

DOI: 10.1039/d5sm00487j

rsc.li/soft-matter-journal

Introduction

Liquid–liquid phase separation plays important roles in the formation of composites,[1] and biological condensates.[2] When the condensing phase forms an isotropic liquid, condensate droplets grow as spheres as a consequence of surface tension with the residual solution. Some of these phase separating systems can form condensates with liquid crystalline ordering, including those of biological condensates and coacervates,[3–5] biomaterials,[6] and nanocomposites.[7–10] In these settings, liquid–liquid crystal phase separation (LLCPS) produces condensate droplets whose interfacial shape is determined by a balance of interfacial tension and elasticity associated with the microstructure of the liquid crystal mesophase within the droplet interior.

In some cases, isotropic–isotropic phase separation precedes the formation of liquid crystal phases,[11] often resulting in macrophase separation.[12] In other cases, demixing droplets immediately nucleate as a liquid crystal mesophase,[13] and the resulting elasticity and defect structure of the liquid crystal mesophase under this confinement[14] can slow or halt phase separation dynamics.[15–17] Such kinetic trapping can entrain droplets of the isotropic phase[13] or colloids, resulting in composite gels.[18] Kinetic trapping can similarly stabilize liquid crystal shells around isotropic microdroplets,[19–22] and sheathing or core layers within electrospun fibers.[23–25]

For liquid crystals with sufficiently large elastic constants, the interface of demixing droplets can reshape to reduce elastic stresses associated with mesophase distortion, resulting in non-spherical droplets.[26] For example, droplets containing nematics and cholesterics can form tactoids,[5,27,28] tori,[29] and surface facets.[30] For such systems, the rate of cooling through a thermotropic phase boundary or rate of concentrating through a lyotropic phase boundary can strongly alter the droplet morphologies that nucleate and persist,[31,32] which can be further complicated by competing flow dynamics.[33,34]

Demixing smectic liquid crystals can form particularly intriguing morphologies, in part because large compression moduli add further constraints on droplet nucleation and growth.

[a] *Department of Chemical and Biomolecular Engineering, University of Pennsylvania, USA. E-mail: cosuji@seas.upenn.edu; Tel: +1-215-573-3608*
[b] *Research Division, ExxonMobil Technology and Engineering Company, Annandale, NJ 08801, USA*
[c] *Department of Physics and Astronomy, University of Pennsylvania, USA*
† Equal contribution authors.

In some cases, demixing smectic condensates can form striking filamentous condensates, which relieve bend distortions in the smectic layers.[35,36] When subjected to sufficiently fast thermal cooling rates, rapidly elongating filaments buckle periodically,[37,38] driven by a balance of hydrodynamic drag and filament bending rigidity.[39] This filamentous growth is reminiscent of behavior in some other systems with anisotropic fluid structuring. For example, similar filament buckling can be observed during shape transformations of liquid crystalline droplets in immiscible aqueous–surfactant–liquid crystal systems,[40,41] reentrant phase growth during the isotropic–smectic transition of some single-component smectogens,[42–44] and growth of myelin figures in surfactant solutions[45–47]—though the underlying driving forces in these systems are distinct.

Liquid–liquid crystal phase separation of smectics can also give rise to more complex droplet shapes, including ribbons, spirals, tori, and flat drops.[35,36,48] Our recent work showed that the interaction of some such systems can form sparse networks with life-like dynamics, driven by the emergent active stresses of filament growth and retraction into flat drops.[49] While these systems exhibit a rich diversity of architectures and dynamics, it remains poorly understood what underlying physical forces dictate the preference for phase separation into specific geometries.

Here, we reveal how the phase behavior of smectogen and solvent blends control the formation of geometrically complex condensate architectures by systematically adjusting their concentrations and molecular structure. We observed a diversity of structures—including filaments, flat drops, and helical coils in addition to commonly observed structures including focal conics and oily streaks—which arose under distinct compositions and concentrations. To better understand the conditions that give rise to different structures, we used differential scanning calorimetry and X-ray scattering to map out the phase behavior. We found that distinct variations in condensate morphology are closely linked to the solvent solubility, as measured by smectic layer swelling and estimated Hansen solubility parameters. Solubility differences likely arise from changes in solvent–smectogen and smectogen–smectogen intermolecular interactions. For some phase separating mixtures, solvent solubility increased with subcooling, resulting in sustained condensate growth within the binodal region. This interpretation was supported by an observed absence of these complex architectures and dynamics in mixtures lacking this solvent swelling behavior. For mixtures that do exhibit sustained solvent swelling, the resulting swelling of smectic layers by solvent likely reduces the bending rigidity of the smectic. Consistent with this interpretation, these mixtures yielded more structurally-complex shapes like helices and coils, and exhibited more rapid rearrangement dynamics that directly suggest larger bending rigidity of smectic layers. This work provides insights on how the composition and concentration of smectogen and solvent influence the diverse dynamics and architectures that arise during the phase separation of liquid crystals.

Results

We investigated the morphology of liquid–liquid crystal phase separation from different binary mixtures of a smectogen and a solvent. We used two different smectogens: 12OCB (4′-cyano-4-*n*-dodecyloxy-biphenyl) and 8OCB (4′-cyano-4-*n*-octyloxy-biphenyl); and five different solvents: squalane (SqA), squalene (SqE), 1-chloronaphthalene, tetradecane, and tetradecylbenzene (Fig. 1A) (SI 1. Chemicals). Binary mixtures were loaded into Hele-Shaw cells constructed from glass cover slips and imaged using polarized optical microscopy (Fig. 1B) (SI 4. Imaging). Consistent with previous literature, we saw binodal phase separation that resulted immediately in a dispersed condensate phase with smectic order. The morphology of these condensates adopted metastable filamentous structures upon growth, which in many cases underwent additional shape transformations to form a range of more complex morphologies (Fig. 1C). We investigated the diversity in these metastable condensate morphologies using imaging, X-ray scattering, and differential scanning calorimetry as a function of temperature, concentration, and solvent choice.

Binary mixtures of 12OCB and SqA form sparse networks

We first investigated the liquid–liquid phase separation of 12OCB and SqA during constant cooling into the binodal region at 1 °C min^{-1}. For a solvent fraction of ω = 0.61, we saw the formation of sparse networks composed largely of filaments and flat drops (Fig. 1D and Movie S1). These morphologies are consistent with our previous observations at a lower solvent fraction of ω = 0.55.[49] For both solvent fractions, condensates grew as rapidly-elongating filaments with homeotropic anchoring at the liquid interface that results in radial splay of the smectic director field—and equivalently, bend in the smectic layers (Fig. 1C). The formation of filaments, rather than spheres, is driven by a reduction in the elastic distortion energy associated with smectogen splay,[44] characterized by the Frank–Oseen distortion energy, $F_e = \pi K l \ln(R/R_c)$, where K is the bend modulus of smectic layers, l is the filament length, R is the filament radius, and $R_c \sim 0.1$ nm is the radius of a defect core running along the filament centerline, estimated to be on the order of the molecule size. Filaments are buckled by hydrodynamics during elongation.[38,39] As filaments continue to grow, they densify from an imbalance of exponential growth and quadratic dispersion,[49] eventually resulting in collapse to form bulged discs with undistorted interiors (Fig. 1C), which form the nodes of the condensate network architecture. Filament growth and network formation occurred only during cooling; reheating the condensate networks resulted in network shrinkage.[49]

For this higher solvent fraction of ω = 0.61, we additionally saw many filaments wind with themselves to form helices (Fig. 1E) or wrap around thicker filaments to form coils (Fig. 1E, arrow in Fig. 1D). Formation of helices and coils was present in ω = 0.55, but at a much lower prevalence. Preliminary work suggests that these coiled motifs are not the result of any chiral mesophase transition, as our system notably lacks

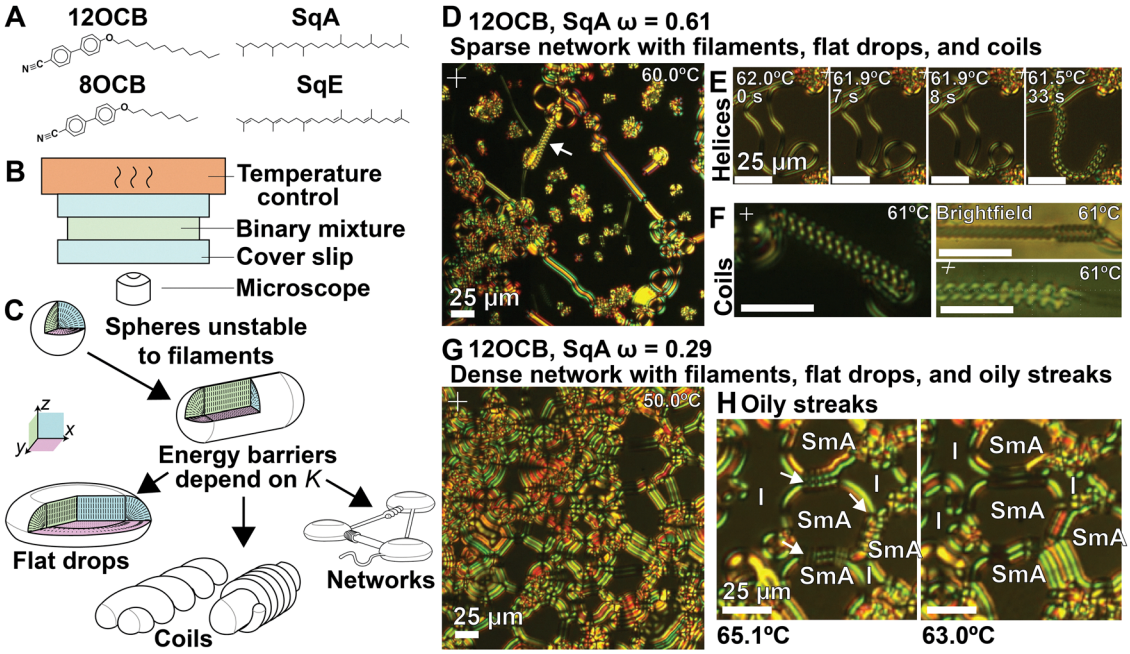

Fig. 1 Diversity of condensate geometries for different solvent concentrations in 12OCB SqA mixtures. (A) Binary mixtures containing one mesogen (12OCB or 8OCB) and one solvent (SqA or SqE) at varying concentration were prepared above the clearing temperature, at which they are fully miscible. (B) Mixtures were placed between glass slides on a thermal stage and cooled from the clearing temperature at 1 °C min^{-1} and imaged using a polarized optical microscope. (C) Schematic of some observed condensate geometries. Smectic microstructure of filaments and bulged discs were inferred from birefringence (SI. 2 Imaging). (D) Phase separation of 12OCB and a high SqA solvent mass fraction of ω = 0.61 resulted in a sparse network comprised of filaments, bulged discs, helices, and coils. The formation of a smectic A (SmA) mesophase[49] produced visible birefringence under crossed polarizers. (E) Time sequence of filament self-contacting, transiently forming an adhesive contact, and rapidly winding to form double helix. (F) Snapshots of coiled structures observed, comprised of one filament wrapped around a straight filament (left) or transitioning between a double helix and a coil (right images). The upper right image was collected under brightfield, without polarizers. (G) 12OCB with a lower SqA solvent mass fraction of ω = 0.29 resulted in a denser network of filaments and bulged discs, which formed commonly-observed oily streaks where they contacted each other (white arrows). (H) Close up of oily streaks which formed upon contact of bulged disc domains, which eventually coarsened (right). All scale bars indicate 25 μm.

any molecular chirality or bent-core mesogens.[50,51] Instead, these structures seem to arise from the partial coalescence of filaments. In all recorded cases, coils formed directly from filaments during rapid rearrangement events, which our imaging did not resolve. Coils were observed co-existing with filaments and other structures at all temperatures, and in some cases were observed rearranging further into more complex morphologies or flat drops; further supporting the interpretation that they are an intermediate metastable condensate morphology. Characterizing the energetics of this coiling requires a careful investigation of the internal mesophase structure of these coils, which we did not investigate here. Nevertheless, we hypothesize that the activation barrier to form coiled domains requires at least an initial high-curvature bending of filaments, resulting in a large penalty to the distortion energy F_e. We thus expect these coiled motifs to arise and persist more when the bend modulus of the smectic layers K is sufficiently low.

We confirmed this trend by repeating this experiment at a lower solvent fraction ω = 0.29. We again saw the growth of filaments and bulged discs, but did not observe any coiling—consistent with our interpretation that the bend modulus K is higher at lower solvent fractions. At this concentration, the higher volume fraction of the condensate phase causes the network to be significantly more compact (Fig. 1G). As bulged discs grew, they contacted each other directly forming textures consistent with commonly-observed oily streaks. These oily streak textures zippered together (arrows in Fig. 1H and Movie S2) before coarsening to layered contacts, likely driven by surface tension and potentially relaxation of the smectic mesophase distortion. While we do not characterize the zippering dynamics of these contact regions, we anticipate that the zippering velocity similarly depends on the bend modulus K and the viscosity of the isotropic fluid μ, motivated by our characterization of filament retraction into flat drops.[49] However, dynamics of oily streak formation are also expected to depend on the energy of edge dislocations, and dislocation unbinding kinetics.[52,53]

Characterization of solvent partitioning into smectic layers

We hypothesize that the observed variations in condensate geometry reflect differences in smectic microstructure that influence the bulk bending rigidity. We characterized this microstructure using small- and wide-angle X-ray scattering (SAXS and WAXS, respectively) as a function of temperature and concentration (SI 3. X-Ray scattering). Upon cooling from the isotropic phase, differential scanning calorimetry (DSC) showed exothermic peaks concomitant with changes in the

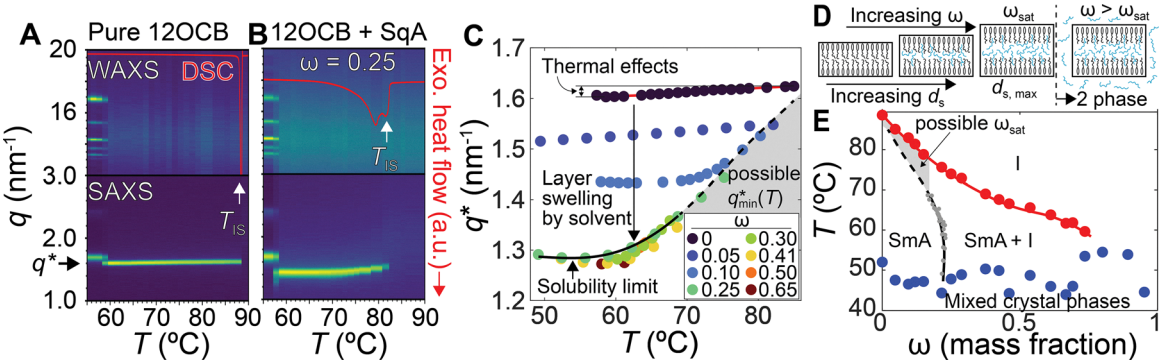

Fig. 2 Phase behavior of 12OCB SqA mixtures. (A) Small-angle X-ray scattering (SAXS, lower panel) and wide-angle X-ray scattering (WAXS; upper panel) of pure 12OCB, and (B). 12OCB and 10 wt% SqA. A sharp dominant peak q^* appeared upon formation of a smectic phase. Differential scanning calorimetry (DSC; red line) shows phase changes that align with structural changes in SAXS and WAXS. (C) Smectic layer swelling by solvent is visible from shift in dominant scattering peak q^*. Measurements of $q^*(T)$ for pure 12OCB show thermal-effects are negligible. (D) Schematic of solvent uptake into smectic layering, increasing layer spacing which plateaus at the solubility limit. (E) Phase diagram measured from exothermic peaks in DSC (red and blue points). Red and blue lines are to guide the eye. Identity of different phases between DSC peaks assessed by temperature-dependent SAXS and WAXS data. The black line was computed exactly from eqn (2). Dashed portion of line indicates lower bound for ω_{sat}, computed from the dashed portion of line in panel D, where insufficient data makes it unclear whether the minimum observed q^* is the true minimum.

scattering features, verifying the presence of phase changes (red overlays) (SI 4. Differential scanning calorimetry).

Pure 12OCB transitioned directly from an isotropic liquid to a smectic A liquid crystal at $T_{IS} = 89$ °C, characterized by a sharp exothermic peak in the DSC data (Fig. 2A red line) and a sharp scattering peak q^* in the SAXS profile (Fig. 2A green and yellow in heat map). The sharp scattering peak provides a measure of the smectic layer spacing $d_{S,0} = 2\pi/q^* \approx 3.9$ nm, which did not vary appreciably with temperature. Beneath $T_{SC} = 52$ °C measured by DSC, pure 12OCB transitioned to a crystalline phase, which we did not analyze.

Upon addition of the solvent squalane (SqA), the isotropic–smectic transition temperature was depressed, and the scattering peak q^* decreased with temperature (Fig. 2B), suggesting that the solvent can swell the smectic phase, dilating layers up to $d_S \approx 4.8$ nm (23% increase). The gradual decrease of q^* during subcooling suggests that the solubility of the solvent in the smectic phase is a function of temperature. We measured this solubility of the solvent in the smectic phase by repeating these measurements for a range of smectogen–solvent concentrations (Fig. 2C). The layer swelling was more extreme for higher solvent concentrations, but saturated along a manifold of minimum q^*, reflecting this solubility limit (black curve in Fig. 2C). Saturation above $\omega = 0.25$ provides an upper bound for the solubility limit; measurements at $\omega = 0.10$ exhibiting lesser layer swelling provide a lower bound for the solubility limit.

We estimated the solubility limit more precisely by calculating the volume fraction of solvent consistent with the observed layer swelling along this manifold $q^*_{min} = 2\pi/d_{S,max}$. At the solubility limit ω_{max}, the smectic phase spanned the system, *i.e.* there was no residual solvent (Fig. 2D). Thus, neglecting any nonideal volume change of mixing, the volume fraction of solvent within the smectic phase from the layer swelling is:

$$\phi_{max}(T) \approx \frac{d_{S,max}(T) - d_{S,0}(T)}{d_{S,max}(T)}, \quad (1)$$

where $d_{S,0}$ was estimated using a spline interpolation of the $q^*(T)$ of the pure 12OCB (black points and red spline in Fig. 2C); and $d_{S,max}$ was estimated from the $q^*(T)$ data points that fall along the minimum manifold (black spline labeled "solubility limit" in Fig. 2C). The corresponding mass fraction is by definition:

$$\omega_{sat}(T) = \phi_{max}(T)\left(\frac{\rho_S}{\rho_{Av}}\right), \quad (2)$$

where the density of the pure solvent SqA is $\rho_S = 0.81$ g cm^{-3},[54] and the average density along the manifold is by definition $\rho_{Av} = \rho_S\phi_{max} + \rho_M(1 - \phi_{max})$. We measure the density of the pure mesogen 12OCB to be $\rho_M \approx 0.7$ g cm^{-3}. The resulting boundary provides a measure for the solvent concentration of the dispersed smectic condensate when the system is in the two-phase region. The predicted solvent solubility in the smectic phase increases with temperature to a maximum of ω_{sat} ($T \approx 50$ °C) $\approx$ 0.23, consistent with the directly measured upper (<0.25) and lower (>0.10) bounds. For $T > 67$ °C, we did not have sufficient data points to ensure the minimum measure q^* coincides with a ω above the saturation at that temperature, so we plotted the apparent manifold (black dashed line in Fig. 2C), which indicates a lower bound solvent concentration in the smectic.

From these measurements, we constructed the phase diagram for 12OCB squalane (Fig. 2E), using DSC to measure T_{IS} and T_{SC} (red and blue points, respectively; red and blue lines are drawn to guide the eye). We used SAXS and WAXS profiles to identify the phase within each region. We drew the phase boundary between the single-phase smectic A and the two-phase region using the solubility limit computed from eqn (2) (black line Fig. 2E). We expected from the curvature of the solvent solubility boundary suggests that demixing smectic condensates would become more solvent-swollen as they cool, presumably reducing filament rigidity and allowing the formation of more contorted helical and coiled condensate geometries observed (Fig. 1D–F).

Characterization of smectic condensate demixing in solvents with lower solubility

The important role of smectic layer swelling by solvent uptake suggests that condensate rigidity, and hence structure, may be sensitive to the choice of solvent. We investigated this sensitivity by comparing the phase behavior of 12OCB with a different solvent, squalene (SqE). Squalene is structurally identical to squalane, but with six unsaturated bonds, which presumably alter the intermolecular interactions with the smectogen 12OCB. Estimation of the Hansen solubility parameters (SI 5. Hansen Solubility Parameters) suggests that SqE should exhibit a lower solubility within the dodecyloxyl tail region of the 12OCB smectic mesophase, with a distance in Hansen solubility space of $R_a = \Sigma c_k(\delta_{k,S} - \delta_{k,A})^2 = 3.5$, as compared to $R_a = 3.2$ for SqA in 12OCB.

Upon phase separation ($\omega = 0.21$), we similarly saw the formation of filaments and flat drops, which form textures consistent with commonly-observed oily streaks when they contact each other (Fig. 3A). At a lower concentration ($\omega = 0.15$) we observed the formation of rounded disc-like domains in contact with the surface (Fig. 3B), which exhibited textures consistent with focal conic domains.[55,56] Such focal conics are commonly-observed for smectics in direct contact with flat substrates with homeotropic anchoring (SI. 2 Imaging), forming as a result of inherent frustration between flat smectic layers in the vicinity of the flat substrate, and curved layers in the vicinity of the curved fluid interface.[57] Filamentous protrusions grew from these surface-contacting domains. At all concentrations of SqE, growing filaments collapsed and retracted rapidly when they contacted other filaments or themselves, even at low filament density, resulting in full retraction in <1 s, faster than our imaging resolved (Movies S3 and S4). We did not see the formation of coils at any concentration of SqE, further suggesting that the presence of SqE results in a higher bending rigidity. Motivated by the observed dependence of rigidity on solvent swelling in the presence of SqA (Fig. 2E), we hypothesized that SqE is less soluble with 12OCB, resulting in reduced layer swelling and higher bending rigidity of smectic layers.

We again used SAXS and WAXS (Fig. 3C) to measure shifts in the scattering peak q^* (Fig. 3D). In conjunction with DSC, we mapped the phase diagram (Fig. 3E). We again used the shift in q^* to infer swelling of the smectic layers by the solvent SqE, which saturated along the manifold shown by the black line in Fig. 3D. Using the density of SqE $\rho_S = 0.858$ g cm^{-3} in eqn (2) provides the boundary between the smectic and two-phase region (black line in Fig. 3E). The maximum content of SqE in the smectic layers is $\omega_{max} \approx 0.18$, confirming our expectation from Hansen solubility parameter estimates that SqE is less soluble in the smectic than SqA. We expected this reduction in solvent swelling to result in more compact smectic layers with a higher bending rigidity. Consistent with this interpretation, 12OCB SqE mixtures exhibited the formation of filaments and flat drops as well as commonly-observed oily streaks, but did not form coils at any concentration—presumably because such coils require stronger bending of the smectic phase.

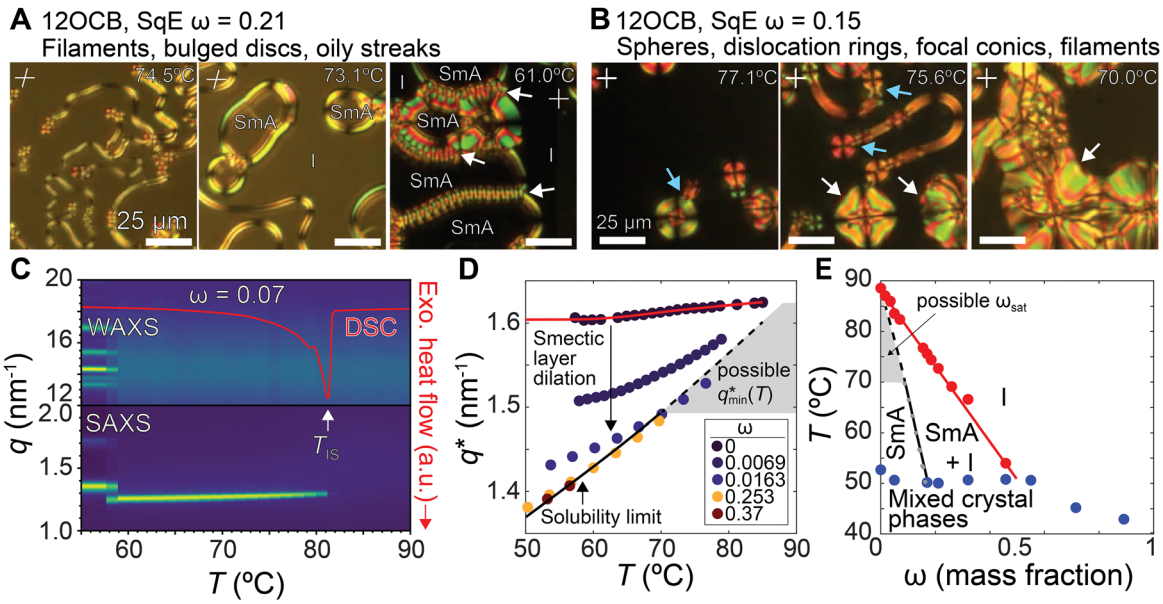

Fig. 3 Higher rigidity structures in 12OCB SqE mixtures. (A) 12OCB with a large fraction $\omega = 0.21$ of SqE phase separated to form liquid crystalline filaments and bulged discs, which formed oily streaks where they contact each other (white arrows). Image collected under partially-crossed polarizers. (B) 12OCB with a smaller fraction $\omega = 0.15$ of SqE formed droplets with strong contact with the glass substrate resulting in dislocation ring textures, sometimes with filamentous protrusions (blue arrows) and focal conic domains (white arrows). All scale bars indicate 25 μm. (C) SAXS and WAXS data for $\omega = 0.07$ (D) Smectic layer swelling. Black line indicates manifold of q^*_{min} from above solvent saturation limit. Dashed line indicates upper bound for q^*_{min} from current measurements, which may not be at $\omega_{sat}(T)$. (E) Phase diagram inferred from exothermic peaks in DSC (red and blue points). Red and blue lines drawn to guide the eye. Black line computed directly from eqn (2). Dashed line corresponds to lower bound ω_{sat}, which was inferred from upper bound q^*_{min} marked by dashed line in panel D. Identity of different phases between DSC peaks assessed by temperature-dependent SAXS and WAXS data.

To validate our hypothesis that reduced solvent swelling increases the bending rigidity of smectic layers K, we compared the retraction speeds of filaments into flat drops. For the SqA-swollen smectic, high speeds $U < 100$ μm s^{-1} near the end of retraction provides a simplified expression of our previously proposed model[49] $U = K\ln(R/R_c)/(8\mu cl)$, where the unknown constant c combines the anisotropic drag on a slender body and the fraction of the buckled filament that contributes to the drag.[39] In the SqE system, our limited imaging resolution instead provided a lower-bound on retraction velocities, for which we observed $U > 650$ μm s^{-1}. From this difference, we inferred a relative change in K between the SqA and SqE swollen smectic from this change in velocity, assuming similar values of c. This estimate suggests that the SqE-swollen 12OCB smectic has a bend modulus $K > 7$ to 14× higher than the SqA-swollen smectic—supporting our interpretation that the reduced solvent swelling by SqE leads to increased smectic layer bending rigidity. Thus, relatively modest changes in solvent–smectogen interaction can strongly influence the architecture of condensates during phase separation by altering the bending rigidity of solvent-swollen smectic layers.

Qualitative comparison of condensate morphologies to other solvents with lower solubility

To further demonstrate the strong dependence on solubility, we tested several other solvents with lower solubility than SqA: tetradecane, tetradecylbenzene, and 1-chloronaphthalene. Similar estimation of Hansen solubility parameters (SI 5. Hansen Solubility Parameters) gave distances in Hansen solubility space of R_a = 3.2, 3.3, 3.4, 3.5, and 9.0 for squalane, tetradecane, tetradecylbenzene, squalene, and 1-chloronaphthalene, respectively (Table S1).

We compared the condensate morphologies obtained for these different solvents under identical cooling conditions (1 °C min^{-1}) for similar weight fractions $\omega \sim 0.2$ with 12OCB. Consistent with our expectation, solvents with higher miscibility (lower R_a) exhibited more filamentous and coiled structures that assemble into networked morphologies (Fig. 4A and B), while solvents with lower miscibility formed primarily flat drops in contact with the glass substrates, with oily-streak-like textures between contacting flat drops (Fig. 4C and D). The solvent with a much lower miscibility, 1-chloronapthalene, instead exhibits phase separation into droplets with high sphericity and focal conic textures, similar to commonly-observed textures in phase separated smectics (Fig. 4E).

Characterization of condensate morphology in system exhibiting an intermediate nematic phase

These observations suggest that these nonequilibrium condensate morphologies depend sensitively on the pathway taken through phase space. We further tested this using 8OCB, a similar mesogenic liquid crystal with a shorter alkyl tail (Fig. 1A). Shorter alkyl tails exhibit lower bending rigidities K, making filamentous and networked architectures more accessible. However, 8OCB exhibits a more complex phase behavior that alters the pathway to form smectic condensates. Similar use of SAXS, WAXS, and DSC demonstrates that pure 8OCB undergoes an isotropic–nematic transition at T_{IN} = 79.3 °C, a nematic–smectic A transition below T_{NS} = 65.9 °C, and a smectic A to crystal transition below T_{SC} = 45 °C (Fig. 5A). We tested whether this variation in pathway taken through phase space altered the morphology of condensates formed.

We used SAXS, WAXS, and DSC (Fig. 5B) to map the phase diagram for 8OCB-SqA binary mixtures (Fig. 5C). At low concentrations of SqA $\omega < 0.18$, the nematic–smectic transition occured within the single-phase region, *i.e.* the smectic was system-spanning at T_{NS}, so there were no smectic condensates to analyze (Fig. 5D and Movie S5).

At higher concentrations of SqA $\omega > 0.18$, the binary mixture underwent a sequence of phase transitions over a narrow temperature range: first undergoing liquid–liquid phase separation to form two isotropic liquids, then undergoing an isotropic to nematic transition in one of the liquid phases, and then a nematic to smectic transition in the same phase (Fig. 5E and Movie S6). Since 8OCB should exhibit lower K, condensates should exhibit similar filamentous and networked morphologies if they were purely equilibrium phase separated structures. We instead hypothesized that the altered

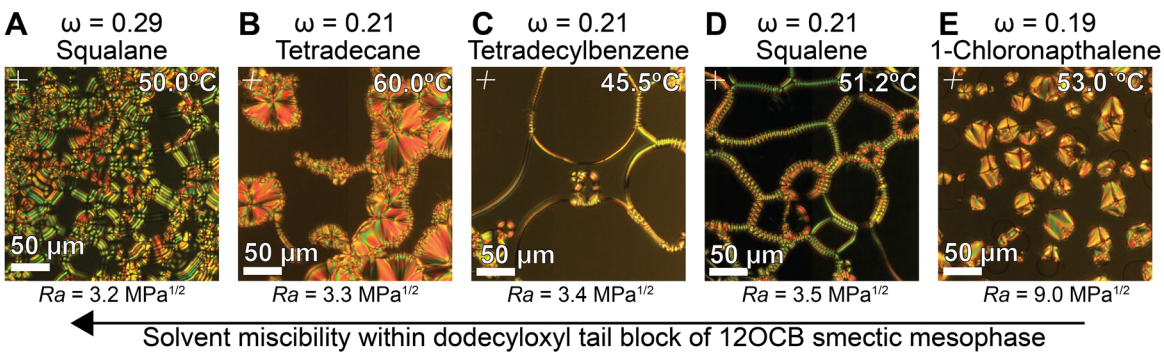

Fig. 4 Comparison of condensate morphologies obtained for 12OCB mixtures with varying solvents. All samples cooled at 1 °C min^{-1} and imaged under crossed or partially-crossed polarizers. Solvents ordered by decreasing miscibility within the dodecyloxyl tail block region of the 12OCB smectic, as determined by increasing distance in Hansen Solubility space R_a: (A) squalane R_a = 3.2 MPa$^{1/2}$; (B) tetradecane R_a = 3.3 MPa$^{1/2}$; (C) tetradecylbenzene R_a = 3.4 MPa$^{1/2}$; (D) squalene R_a = 3.5 MPa$^{1/2}$; (E) 1-chloronapthalene R_a = 9.0 MPa$^{1/2}$.

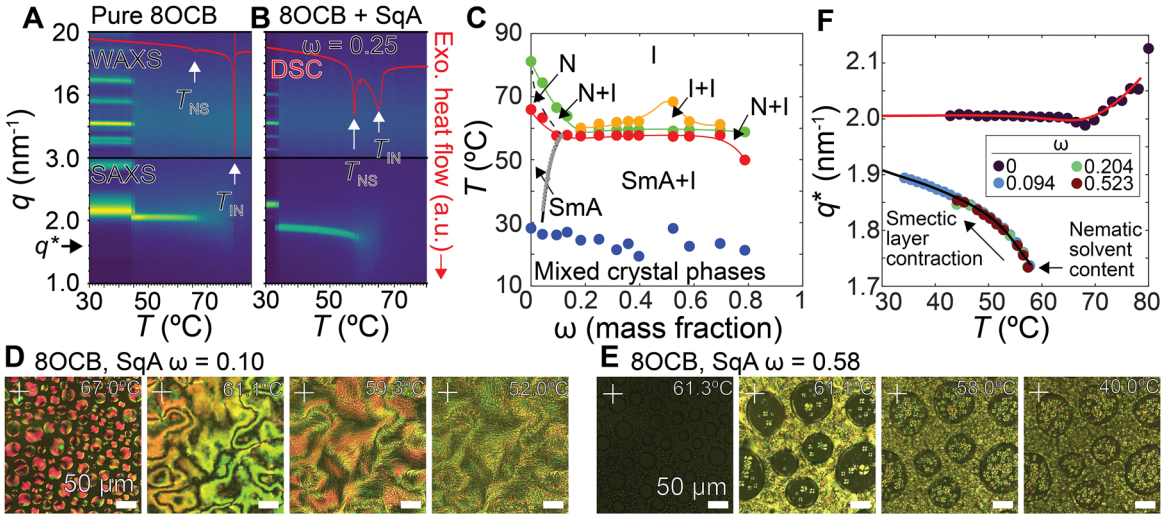

Fig. 5 Lack of filaments in 8OCB SqA mixtures. (A) SAXS (lower panel) and WAXS (upper panel) of pure 8OCB. The diffuse q^* peak in the nematic phase represents the weak positional correlation of nematogens. The pronounced q^* peak in the smectic phase indicates a layer spacing $d_S = 2\pi/q^* \approx 3.1$ nm. (B) SAXS, WAXS, and DSC profiles for 8OCB and SqA at $\omega = 0.1$. (C) Phase diagram constructed from SAXS and DSC. Red, green, and yellow lines are drawn to guide the eye. Black line was determined from minimum q^* of smectic phase using eqn (2) the isotropic–isotropic phase separation was discerned from exothermic peaks in DSC, the absence of structural peaks in SAXS and WAXS, and the formation of droplets visible in brightfield that did not exhibit birefringence. The isotropic–nematic transitions are discerned from exothermic peaks in DSC and a diffuse q^* scattering peaks in SAXS. (D) Phase separation through the I + N region resulted in nematic spheres, which coalesced until they spanned the system, then transitioned to a system spanning smectic. When the system passed into the 2-phase region, dispersed isotropic droplets formed, which were too small to resolve optically. The absence of a dispersed smectic condesate precluded the observation of filaments or sparse networks at this concentration. (E) Phase separation through the I + I region resulted in isotropic droplets in an isotropic continuous phase, followed by an isotropic–nematic transition that resulted in significant phase rearrangement. At $T_{NS} \approx 58$ °C the dispersed nematic droplets transitioned into a smectic mesophase; a slight change in optical texture visible was visible in panel 3 and Movie S6. These dispersed smectic condensate droplets remained spherical and shrunk slightly during cooling. All scale bars indicate 50 μm. (F) Shift in q^* for smectic phase. Initial solvent content in nematic phase resulted in a smectic phase with layers swollen ~19% above that of pure 8OCB. Upon further cooling, increasing q^* indicates layers shrunk to expel solvent, resulting in layer contraction with cooling.

phase space pathway would disrupt the formation of filamentous and networked architectures, which would further support that these morphologies are nonequilibrium metastable structures.

Upon transition from nematic to smectic mesophase beneath T_{NS}, the 8OCB smectic condensates remained spherical and shrunk gradually upon further cooling without forming any filaments or more complex condensate morphologies (panels 3 and 4 of Fig. 5E and Movie S6). We rationalize this path-dependent behavior using similar solvent swelling measurements. Beneath T_{NS}, the SAXS scattering peak q^* indicates that the nematic phase is highly swollen by the solvent SqA, resulting in an initial smectic layer spacing of $d_s \approx 3.7$ nm in the presence of SqA, compared to $d_S \approx 3.1$ nm for the smectic phase of pure 8OCB (Fig. 5F). The lower smectic bend modulus expected for pure 8OCB, in conjunction with the comparable ~19% layer swelling, both suggest these smectic condensates of 8OCB and SqA should be able to form complex condensate architectures. However, further cooling decreases the solvent content of the smectic layers, producing differential contraction of layers during cooling. This smectic layer contraction is in direct contrast to the 12OCB with SqA and SqE mixtures, for which solvent content of the smectic layers increased with cooling, producing differential swelling of layers during cooling. The inverted solvent swelling behavior of the 8OCB with SqA smectic phase causes the smectic condensates to shrink, rather than grow. Thus, the observed absence of filaments in this system is consistent with the proposed microscopic mechanism that spherical smectic condensates are unstable to filaments upon growth.[35,49] The evolution of filaments into higher-order flat drops, coils, and networks thereof likely relies on similar path-dependent growth dynamics. Together, these observations highlight the importance of both smectic bending rigidity and growth dynamics on the formation of complex condensate architectures.

Discussion

This work highlights a diverse range of nonequilibrium condensate morphologies accessible during the liquid–liquid crystal phase separation (LLCPS) of smectic condensates. We found that the geometry of dispersed liquid crystalline droplets is highly sensitive to the choice of smectogen, solvent, and concentration during cooling. In some cases, these condensates can form spatially-sparse 2D networks composed of filaments, flat drops, and sometimes coils. These networks remain open to form bicontinuous smectic and isotropic fluid phases. X-ray scattering measurements at varying solvent content suggest that these differences in droplet geometry evolution are in large part correlated with changes in solvent content within the smectic layers. Higher solvent content in smectic layers

apparently decreases the smectic layer bending rigidity K, favoring filaments and coiled motifs. Lower solvent contents correlate with more sensitive collapse of filaments into flat drops, which can additionally form more commonly-observed structures consistent with oily streaks focal conics. The stability of filaments and coiled motifs at higher solvent fractions seems crucial to forming and maintaining the spatially-sparse networks.

For some conditions, we observed the formation of coiled motifs, whereby filaments wind around themselves or other filaments. It is unclear why these coiled motifs form, and how they remain stable—particularly because the smectogen (12OCB) is neither chiral nor bent. However, it is apparent that formation of these coiled motifs is associated with an energy barrier related to the curvature required to bend the constituent filaments along the tight helical tube. Since this helical curvature is often on the order of the inverse filament radius $\sim {R_F}^{-1}$ and the persistence length of the filaments is often $\sim$100's of R_F, we anticipate these barriers to be large and sensitive to changes in the smectic layer bending rigidity K. Characterizing the internal mesophase structure and energetics of these coils remains an important direction for continued work.

Our work further demonstrates that the coexistence of a smectic liquid crystal and isotropic liquid is a necessary but insufficient condition to form condensate networks. As demonstrated by our tests in binary mixtures of 8OCB and SqA, neither filaments nor their networks were observed when initially-spherical smectic condensates shrink during cooling ($\omega >$ 0.18). These observations indicate that the formation of filaments, and their subsequent linkage into networks, inherently requires growth of a dispersed smectic condensate. The requirement of growth in the dispersed phase further suggests that these complex architectures are metastable, path-dependent morphologies of the liquid crystal. Though all dispersed droplets are inherently metastable compared to the macroscopic phase separation, the stability of architectures with highly distorted liquid crystal microstructures for hours suggests that this process may be a more general route to assemble complex out-of-equilibrium structures.

Together, our results suggest the importance of solvent choice on the metastable condensate morphologies formed during smectic demixing. When solvents with low solubility in the smectic demix, relatively simple condensate morphologies are formed, exhibiting commonly-observed focal conic and oily streak textures. In contrast, solvents with increasing solubility within the smectic can swell smectic layers (as measured by X-ray scattering), thereby reducing the bend modulus K (as estimated from filament reeling velocities). As a result, smectic condensates with high solvent contents can maintain metastable condensate morphologies with more complex structures with larger degrees of layer bending—including networks of filaments, coils, and flat drops. Given the diversity of droplet morphologies observed from relatively modest changes in mesogen choice, solvent choice, and growth pathways, we anticipate a broad design space of architectures could be accessed in liquid crystalline condensates, for example in condensates of biomacromolecules[5,28] and the formation of biomaterials.[6]

Author contributions

Y. M., P. A. H., and C. O. O. designed research; Y. M. and N. K. K. performed research; C. A. B., Y. M., P. A. H. and C. O. O. analyzed data; M. G. and E. B. S. acquired funding; M. G., E. B. S., and O. A. reviewed and edited the paper; Y. M., M. G., E. B. S., and C. O. O. conceptualized the project; and C. A. B. and C. O. O. wrote the paper.

Conflicts of interest

There are no conflicts to declare.

Data availability

All data relevant to this work are included in the main text, or on the publicly accessible online repository **https://github.com/cabrowne/StructuralDiversity**.

Movies are available on the publicly accessible online repository **https://github.com/cabrowne/StructuralDiversity.** Movie 1. Phase separation of 12OCB and SqA (ω = 0.61) when cooled 67 °C to 60 °C at 0.43 °C min^{-1}. Imaging switches between 5×, 20×, and 63× magnification (field of view 1480 μm, 370 μm, and 117 μm, respectively). Captured at an average 0.82 fps, playback approximately 37× real time (temperature overlays exact). Imaging switches between brightfield (light background) and fully-crossed polarizers (dark background) to aid in identification of structures. Growth of filaments and collapse into bulged discs formed sparse condensate network. Filaments dynamically wound and unwound to form helical and coiled structures. Movie 2. Phase separation of 12OCB and SqA (ω = 0.29) when cooled 74 °C to 48 °C at 1 °C min^{-1}. Captured under 20× magnification, 370 μm field of view. Captured at an average 0.88 fps, playback approximately 34× real time (temperature overlays exact). Condensates formed filaments which collapsed into bulged discs that formed a dense network. As bulged discs grew and contacted each other, they formed oily-streaks. Movie 3. Phase separation of 12OCB and SqE (ω = 0.21) when cooled 90 °C to 49 °C at 1 °C min^{-1}. Captured under 20× magnification, 370 μm field of view. Captured at an average 0.97 fps, playback approximately 31× real time (temperature overlays exact). Imaging switches between partially-crossed polarizers (lighter background) and fully-crossed polarizers (darker background) to aid in identification of structures. Filaments grew and collapsed to form bulged discs. Bulged discs retracted filaments faster than imaging resolved. As bulged discs contacted, they formed oily streaks, which did not relax. Movie 4. Phase separation of 12OCB and SqE (ω = 0.15) when cooled 85 °C to 50 °C at 1 °C min^{-1}. Captured under 20× magnification, 370 μm field of view. Captured at an average 0.73 fps, playback approximately 42× real time (temperature overlays exact). Birefringent liquid

crystal domains formed defect domain walls in contact with glass substrate, including textures consistent with dislocation rings and focal conic flowers. Movie 5. Phase separation of 8OCB and SqA (ω = 0.10) when cooled 70 °C to 50 °C at 0.78 °C min^{-1}. Captured under 20× magnification, 370 μm field of view. Captured at an average 0.60 fps, playback approximately 50× real time (temperature overlays exact). Circular domains with nematic ordering nucleated and coalesced as they grew until the system became a single continuous nematic phase. A nematic to smectic mesophase transition around 60 °C resulted in a rapid system-wide change in optical texture. No filaments or networks formed. Movie 6. Phase separation of 8OCB and SqA (ω = 0.58) when cooled 65 °C to 40 °C at 1 °C min^{-1}. Captured under 20× magnification, 370 μm field of view. Captured at an average 0.83 fps, playback approximately 12× real time (temperature overlays exact). Circular domains without birefringence nucleated and grew, consistent with two isotropic fluids formed by liquid liquid phase separation. Around 61 °C the continuous phase underwent an isotropic to nematic transition, resulting in partial inversion of the nematic droplets to form dispersed droplets within the dispersed isotropic droplets. The dispersed nematic droplets remained circular. Around 59 °C the nematic droplets underwent a nematic smectic mesophase transition, resulting in a rapid change in the optical texture. Dispersed smectic drops remained circular, except where they contacted each other, forming oily streak textures. No filaments or networks formed. See DOI: https://doi.org/10.1039/d5sm00487j

Acknowledgements

It is our pleasure to thank Jonathan D. Saathoff for insightful discussions. This work was supported by the NSF MRSEC at the Laboratory for Research on the Structure of Matter (LRSM) at the University of Pennsylvania (NSF DMR2309043) and by ExxonMobil Technology and Engineering Company. The Authors acknowledge the use of the Dual Source and Environmental X-ray scattering facility operated by the University of Pennsylvania LRSM (NSF DMR2309043). The equipment purchase was made possible by NSF MRI grant (1725969) and ARO DURIP grant (W911NF-17-1-0282). C. A. B. acknowledges postdoctoral fellowship support from the Center for Soft and Living Matter at the University of Pennsylvania.

References

1 Y. Liu, Polymerization-induced phase separation and resulting thermomechanical properties of thermosetting/reactive nonlinear polymer blends: a review, *J. Appl. Polym. Sci.*, 2013, **127**(5), 3279–3292.
2 Y. Shin and C. P. Brangwynne, Liquid phase condensation in cell physiology and disease, *Science*, 2017, **357**(6357), eaaf4382.
3 M. Nakata, G. Zanchetta, B. D. Chapman, C. D. Jones, J. O. Cross and R. Pindak, *et al.*, End-to-End Stacking and Liquid Crystal Condensation of 6- to 20-Base Pair DNA Duplexes, *Science*, 2007, **318**(5854), 1276–1279.
4 T. Bellini, G. Zanchetta, T. P. Fraccia, R. Cerbino, E. Tsai and G. P. Smith, *et al.*, Liquid crystal self-assembly of random-sequence DNA oligomers, *Proc. Natl. Acad. Sci. U. S. A.*, 2011, **109**(4), 1110–1115.
5 T. P. Fraccia and G. Zanchetta, Liquid–liquid crystalline phase separation in biomolecular solutions, *Curr. Opin. Colloid Interface Sci.*, 2021, **56**, 101500.
6 M. J. Harrington, R. Mezzenga and A. Miserez, Fluid protein condensates for bio-inspired applications, *Nat. Rev. Bioeng.*, 2024, **2**(3), 260–278.
7 T. Matsumoto, Mesophase pitch and its carbon fibers, *Pure Appl. Chem.*, 1985, **57**(11), 1553–1562.
8 H. Yoon, Z. R. Hinton, J. Heinzman, C. E. Chase, M. Gopinadhan and K. V. Edmond, *et al.*, The effect of pyrolysis on the chemical, thermal and rheological properties of pitch, *Soft Matter*, 2021, **17**(39), 8925–8936.
9 K. Kumari, S. Rani, P. Kumar, S. Prakash, S. R. Dhakate and S. Kumari, Study of mesophase pitch based carbon fibers: Structural changes as a function of anisotropic content, *J. Anal. Appl. Pyrolysis*, 2023, **171**, 105961.
10 R. Colby, K. Edmond, D. Mendez and S. Smith, Understanding Nucleation of Mesophase Pitch Tactoids using 4D-STEM, *Microsc. Microanal.*, 2023, **29**(Supplement_1), 274–275.
11 J. Kalabiński, A. Drozd-Rzoska and S. J. Rzoska, Phase Equilibria and Critical Behavior in Nematogenic MBBA—Isooctane Monotectic-Type Mixtures, *Int. J. Mol. Sci.*, 2023, **24**(3), 2065.
12 L. A. Serrano, M. J. Fornerod, Y. Yang, S. Gaisford, F. Stellacci and S. Guldin, Phase behaviour and applications of a binary liquid mixture of methanol and a thermotropic liquid crystal, *Soft Matter*, 2018, **14**(22), 4615–4620.
13 C. G. Reyes, J. Baller, T. Araki and J. P. F. Lagerwall, Isotropic–isotropic phase separation and spinodal decomposition in liquid crystal–solvent mixtures, *Soft Matter*, 2019, **15**(30), 6044–6054.
14 M. Urbanski, C. G. Reyes, J. Noh, A. Sharma, Y. Geng and V. S. R. Jampani, *et al.*, Liquid crystals in micron-scale droplets, shells and fibers, *J. Phys.: Condens Matter*, 2017, **29**(13), 133003.
15 M. Patel, A. Shimizu S, M. Bates, A. Fernandez-Nieves and S. Guldin, Long term phase separation dynamics in liquid crystal-enriched microdroplets obtained from binary fluid mixtures, *Soft Matter*, 2023, **19**(5), 1017–1024.
16 J. P. F. Lagerwall, The good, the bad and the ugly faces of cyanobiphenyl mesogens in selected tracks of fundamental and applied liquid crystal research, *Liq. Cryst.*, 2024, **51**(8–9), 1296–1310.
17 P. Patel M, A. N. Radhakrishnan, L. Bescher, E. Hunter-Sellars, B. Schmidt-Hansberg and E. Amstad, *et al.*, Temperature-induced liquid crystal microdroplet formation in a partially miscible liquid mixture, *Soft Matter*, 2021, **17**(4), 947–954.
18 V. J. Anderson, E. M. Terentjev, S. P. Meeker, J. Crain and W. C. K. Poon, Cellular solid behaviour of liquid crystal

colloids 1. Phase separation and morphology, *Eur. Phys. J. E: Soft Matter Biol. Phys.*, 2001, **4**(1), 11–20.
19 V. Vitelli and D. R. Nelson, Nematic textures in spherical shells, *Phys. Rev. E: Stat. Phys., Plasmas, Fluids, Relat. Interdiscip. Top.*, 2006, **74**(2), 021711.
20 H. L. Liang, S. Schymura, P. Rudquist and J. Lagerwall, Nematic-Smectic Transition under Confinement in Liquid Crystalline Colloidal Shells, *Phys. Rev. Lett.*, 2011, **106**(24), 247801.
21 Y. K. Kim, X. Wang, P. Mondkar, E. Bukusoglu and N. L. Abbott, Self-reporting and self-regulating liquid crystals, *Nature*, 2018, **557**(7706), 539–544.
22 J. Noh and J. P. F. Lagerwall, Topological Defect-Guided Regular Stacking of Focal Conic Domains in Hybrid-Aligned Smectic Liquid Crystal Shells, *Crystals*, 2021, **11**(8), 913.
23 E. A. Buyuktanir, M. W. Frey and J. L. West, Self-assembled, optically responsive nematic liquid crystal/polymer core-shell fibers: Formation and characterization, *Polymer*, 2010, **51**(21), 4823–4830.
24 J. Wang, A. Jákli and J. L. West, Morphology Tuning of Electrospun Liquid Crystal/Polymer Fibers, *ChemPhysChem*, 2016, **17**(19), 3080–3085.
25 A. Sharma and J. P. F. Lagerwall, Electrospun Composite Liquid Crystal Elastomer Fibers, *Materials*, 2018, **11**(3), 393.
26 J. Bechhoefer, L. Lejcek and P. Oswald, Facets of smectic A droplets I. Shape measurements, *J. Phys. II*, 1992, **2**(1), 27–44.
27 M. Bagnani, G. Nyström, C. De Michele and R. Mezzenga, Amyloid Fibrils Length Controls Shape and Structure of Nematic and Cholesteric Tactoids, *ACS Nano*, 2019, **13**(1), 591–600.
28 H. Almohammadi, S. A. Khadem, P. Azzari, Y. Yuan, A. Guerra and A. D. Rey, *et al.*, Liquid–liquid crystalline phase separation of filamentous colloids and semiflexible polymers: experiments, theory and simulations, *Rep. Prog. Phys.*, 2025, **88**(3), 036601.
29 L. Tortora, H. S. Park, S. W. Kang, V. Savaryn, S. H. Hong and K. Kaznatcheev, *et al.*, Self-assembly, condensation, and order in aqueous lyotropic chromonic liquid crystals crowded with additives, *Soft Matter*, 2010, **6**(17), 4157–4167.
30 J. Jeong, Z. S. Davidson, P. J. Collings, T. C. Lubensky and A. G. Yodh, Chiral symmetry breaking and surface faceting in chromonic liquid crystal droplets with giant elastic anisotropy, *Proc. Natl. Acad. Sci. U. S. A.*, 2014, **111**(5), 1742–1747.
31 H. Almohammadi, Y. Fu and R. Mezzenga, Evaporation-Driven Liquid–Liquid Crystalline Phase Separation in Droplets of Anisotropic Colloids, *ACS Nano*, 2023, **17**(3), 3098–3106.
32 H. Almohammadi, S. Martinek, Y. Yuan, P. Fischer and R. Mezzenga, Disentangling kinetics from thermodynamics in heterogeneous colloidal systems, *Nat. Commun.*, 2023, **14**(1), 607.
33 H. Almohammadi, M. Bagnani and R. Mezzenga, Flow-induced order–order transitions in amyloid fibril liquid crystalline tactoids, *Nat. Commun.*, 2020, **11**(1), 5416.
34 H. Almohammadi, S. A. Khadem, M. Bagnani, A. D. Rey and R. Mezzenga, Shape and structural relaxation of colloidal tactoids, *Nat. Commun.*, 2022, **13**(1), 2778.
35 H. Naito, M. Okuda and O.-Y. Zhong-Can., Preferred equilibrium structures of a smectic-A phase grown from an isotropic phase: Origin of focal conic domains, *Phys. Rev. E: Stat., Nonlinear, Soft Matter Phys.*, 1995, **52**(2), 2095–2098.
36 A. Adamczyk, Hard-core liquid crystal fibers. Proc. SPIE 7050, Liquid Crystals XII. 2008;70501A.
37 H. Naito, M. Okuda and O. Y. Zhong-can, Pattern formation and instability of smectic-A filaments grown from an isotropic phase, *Phys. Rev. E: Stat., Nonlinear, Soft Matter Phys.*, 1997, **55**(2), 1655–1659.
38 M. Todorokihara, Y. Iwata and H. Naito, Periodic buckling of smectic-A tubular filaments in an isotropic phase, *Phys. Rev. E: Stat. Phys., Plasmas, Fluids, Relat. Interdiscip. Top.*, 2004, **70**(2), 021701.
39 M. J. Shelley and T. Ueda, The Stokesian hydrodynamics of flexing, stretching filaments, *Phys. D*, 2000, **146**(1–4), 221–245.
40 W. S. Wei, Y. Xia, S. Ettinger, S. Yang and A. G. Yodh, Molecular heterogeneity drives reconfigurable nematic liquid crystal drops, *Nature*, 2019, **576**(7787), 433–436.
41 K. Peddireddy, S. Čopar, K. V. Le, I. Muševič, C. Bahr and S. R. Jampani Venkata, Self-shaping liquid crystal droplets by balancing bulk elasticity and interfacial tension, *Proc. Natl. Acad. Sci. U. S. A.*, 2021, **118**(14), e2011174118.
42 P. Palffy-Muhoray and E. Weinan, Dynamics of Filaments during the Isotropic–Smectic A Phase Transition, *J. Nonlinear Sci.*, 1998, **9**, 417–437.
43 S. L. Arora, P. Palffy-Muhoray, R. A. Vora, D. J. David and A. M. Dasgupta, Reentrant phenomena in cyano substituted biphenyl esters containing flexible spacers, *Liq. Cryst.*, 1989, **5**(1), 133–140.
44 R. Pratibha and N. V. Madhusudana, Cylindrical growth of smectic A liquid crystals from the isotropic phase in some binary mixtures, *J. Phys. II*, 1992, **2**(3), 383–400.
45 L. N. Zou and S. R. Nagel, Stability and Growth of Single Myelin Figures, *Phys. Rev. Lett.*, 2006, **96**(13), 138301.
46 J. R. Huang, Theory of myelin coiling, *Eur. Phys. J. E: Soft Matter Biol. Phys.*, 2006, **19**(4), 399–412.
47 L. Reissig, D. J. Fairhurst, J. Leng, M. E. Cates, A. R. Mount and S. U. Egelhaaf, Three-Dimensional Structure and Growth of Myelins, *Langmuir*, 2010, **26**(19), 15192–15199.
48 A. Adamczyk, Phase Transitions in Freely Suspended Smectic Droplets. Cotton-Mouton Technique, Architecture of Droplets and Formation of Nematoids, *Mol. Cryst. Liq. Cryst.*, 1989, **170**(1), 53–69.
49 Y. Morimitsu, C. A. Browne, Z. Liu, P. G. Severino, M. Gopinadhan and O. Altintas, *et al.*, Spontaneous assembly of condensate networks during the demixing of structured fluids, *Proc. Natl. Acad. Sci. U. S. A.*, 2024, **121**(39), e2407914121.
50 A. Jakli, Ch Lischka, W. Weissflog, G. Pelzl and A. Saupe, Helical filamentary growth in liquid crystals consisting of banana-shaped molecules, *Liq. Cryst.*, 2000, **27**(11), 1405–1409.
51 G. Pelzl, S. Diele and A. Jákli, Helical superstructures in a novel smectic mesophase formed by achiral banana-shaped molecules, *Liq. Cryst.*, 2011, **33**(11–12), 1513–1523.

52 S. Fujii, S. Komura and C. Y. D. Lu, Structural rheology of focal conic domains: a stress-quench experiment, *Soft Matter*, 2014, **10**(29), 5289–5295.
53 S. Fujii, S. Komura and C. Y. D. Lu, Structural Rheology of the Smectic Phase, *Materials*, 2014, **7**(7), 5146–5168.
54 M. S. Sen, P. Brahma, K. Roy Subir, D. K. Mukherjee and S. B. Roy, Birefringence and Order Parameter of Some Alkyl and Alkoxycyanobiphenyl Liquid Crystals, *Mol. Cryst. Liq. Cryst.*, 1983, **100**(3–4), 327–340.
55 D. A. Beller, M. A. Gharbi, A. Honglawan, K. J. Stebe, S. Yang and R. D. Kamien, Focal Conic Flower Textures at Curved Interfaces, *Phys. Rev. X*, 2013, **3**(4), 041026.
56 W. S. Wei, J. Jeong, P. J. Collings and A. G. Yodh, Focal conic flowers, dislocation rings, and undulation textures in smectic liquid crystal Janus droplets, *Soft Matter*, 2022, **18**(23), 4360–4371.
57 C. Blanc and M. Kleman, The confinement of smectics with a strong anchoring, *Eur. Phys. J. E: Soft Matter Biol. Phys.*, 2001, **4**(2), 241–251.